doi:10.20944/preprints202110.0449.v1

*Type of the Paper (Article)*

# Vis and NIR diffused reflectance study in disordered bismuth manganate – lead titanate ceramics

**Andrzej Molak[1,*], Anna Z. Szeremeta[1], Janusz Koperski[1]**

[1] August Chełkowski Institute of Physics, University of Silesia in Katowice, ul. 75 Pułku Piechoty 1, 41-500 Chorzów, Poland.; andrzej.molak@us.edu.pl, anna.szeremeta@us.edu.pl, janusz.koperski@us.edu.pl
* Correspondence: andrzej.molak@us.edu.pl; Tel.: (+48) 32 3497638.

**Abstract:** This work shows a correlation between light reflectance, absorption, and morphologies of series of (1-*x*) BM–*x* PT, ($x$ = 0.0, 0.02, 0.04, 0.08, 0.12, 0.16, 0.24) ceramics composite. The (1-*x*) BM–*x* PT showed features of a black mirror with a low optical energy gap. The measured Vis-NIR diffused reflectance enabled the calculation of the energy gap using the modified Kubelka-Munk function. The estimated energy gap was lower than 1.5 eV related to low reflectance in the Vis-NIR range. Moreover, obtained histograms of grains, using scanning electron microscope, enabled the correlation between grains size and amount of lead titanate. We deduced from the ceramics surface morphology that marked porosity also induced reflectivity of low magnitude. We correlated the magnitude of the energy gap with phases of the BM-PT composite and with the electrical conductivity activation energy reported in the literature. Our results findings opened prospect studied materials for optical applications.

**Keywords:** bismuth manganite, ceramics, composite, lead titanate, optical energy gap, surface morphology, Vis-NIR reflectance.

## 1. Introduction

Perovskite $ABO_3$ oxide materials attract attention for photo-catalytic and solar cells studies. The energy gap, $E_{gap}$, which separates the energies of the valence band maximum and conduction band minimum, determines the material possibilities for such applications [1]. Electronic structure tuning is necessary for many materials to obtain suitable optical $E_{gap}$ demanded for optical applications because it ought to be ~1.5 eV or lower.

The optoelectrical properties of oxides are related to the energies of the valence and conduction band. However, $ABO_3$ structures allow modifying their properties in accord with performed chemical and physical treatment. The $ABO_3$ valence band is formed by oxygen O 2p states hybridized with states of metal 3d, 4d, and 5d placed in the B position. The 4d and 5d metal ions placed in B sublattice usually form a wide gap in the electronic structure. For instance, several perovskite titanates and niobates show insulator $E_{gap}$ larger than 3 eV. Therefore, ultraviolet, UV, light range only is effective for energy harvesting. Contrary, the metal ions from the 3d group provide narrow $E_{gap}$ lower than 1 eV. Moreover, 3d metal ions, *e.g.*, Fe, Mn, Cr, and Co, form the hybridized states in the vicinity of the valence band. Therefore, the $E_{gap}$ decrease in the $ABO_3$ electronic structure related to 4d and 5d ions sublattices can be obtained by suitable doping with 3d metal ions [2–7]. Moreover, oxygen vacancies, $V_O$, states form shallow and deep levels within the $E_{gap}$. However, narrow gap and intra-gap levels markedly affect electrical conductivity and losses [8].

There are several routes to modify the optical $E_{gap}$ of these oxide $ABO_3$ materials. The substitution of the metal ions can lead either to solid solutions or to the formation of precipitates. Minor phases may appear when the solubility limit is overstepped, and/or actually, a transformation of the phases occurs [7,9]. Modification of the electronic structure can be obtained by an additional treatment that can change the concentration of $V_O$ defects. High-temperature annealing in flowing nitrogen gas influences the electronic structure due to redox reactions within the surface layer. Consequently, nitrogen ions embedded in crystal lattice enable decreasing the gap and affect photo-catalytic activity [10–12]. An important class of photonic crystals is formed from two different dielectric and semiconducting materials, providing the $E_{gap}$ tunability, corresponding to a spatially periodic structure. It was shown that reflectance spectra depended on a number of alternate layers and their refractive indices. The active role of the $Mn^{2+}/Mn^{3+}$ in capturing photons in the NIR spectrum in the case of, e.g., multilayer $Bi(Fe_{1-x}Mn_x)O_3$ photonic crystals and doped $TiO_2$ was analyzed [13,14]. Hence, the concept of the photonic crystal suggests the importance of crystal structure ordering and local disorder effects, which can be achieved in Mn-based composite materials.

Especially in this area, the proper material selection is significant because of its excitation efficiency and charge carrier lifetime. Lifetime is related to time to carrier recombination. It is worth noting that this effect is one of desired energy devices property, that is, tunable optical energy gap and time speed of electrical response. These features enable controlling the electrical properties of a device [15,16].

On the one hand, dielectric perovskites provide low electrical conductivity, negligible dielectric losses, and consequently, low absorption efficiency limited to the UV range because of the wide $E_{gap}$. On the other hand, narrow $E_{gap}$, typical for 3d metal ions, offers much better absorption ability, including visible, Vis, and near infra-red, NIR, range. However, narrow $E_{gap}$ and low activation energy determine marked electrical cross-current flow and losses. Therefore, such contradictory features are to be compensated by using proper materials combination. Such expectations would be reached when materials exhibiting different $E_{gap}$ magnitude are combined. Consequently, we assumed that a composite formed from oxide materials, which show large and narrow $E_{gap}$, respectively, would allow us to modify and tune the optical properties because the narrower gap may enhance light absorbance efficiency in the Vis-NIR range.

We have chosen lead titanate, PT, and bismuth manganate, BM, to obtain ceramics composite**.** The motivation was assumed perspective for the application in photovoltaic devices and density power capacitors because of its electronic structure, high permittivity, and short electrical response time. For instance, it was shown that PT thin film would be useful for photo-catalysis [17].

The PT shows a tetragonal *P4mm* phase at room temperature. Ferroelectric-paraelectric phase transition, which occurs in 763 K, points to the high stability of this compound ferroelectric phase. We presumed that PT addition to BM would affect the electronic structure and modify optical $E_{gap}$. PT is the ferroelectric insulator showing measured optical $E_{gap} = 3.4$ eV [18,19]. The occurrence of oxygen vacancies in PT crystal lattice, which usually is inevitable, occurs from technology processing, markedly influences the $E_{gap}$ magnitude. The first-principles calculations using the density functional theory showed the calculated intrinsic band gap is 2.950 eV and that the oxygen vacancies, $V_O$, and doping nitrogen atoms occurrence in PT lattice can lead to the lowered calculated gap value 2.92 eV, consistent with the experimental $E_{gap} = 2.93$ eV [18]. The full potential linearized augmented plane-wave calculation exhibited that oxygen vacancies induce additional in-gap Ti 3d states -1.1 eV below the Fermi energy [20]. Hence, the determined $E_{gap} = 2.6$ eV seems related to the defects subsystem [21]. The defected PT ceramics obtained from hydrothermally grown powder exhibited $E_a = 1.3$-$2.5$ eV of electrical conductivity [22]. The defected PT crystals, showing various disorders, exhibited conductivity Ea, which varied from 0.2 eV to 1.0 eV when temperature increased from 290 to 800 K variance in [23]. Moreover, the Mn-doped PT crystals exhibited optical $E_{gap}$ lowered to 2.0-2.7 eV, attributed to the occurrence of oxygen vacancies, $V_O$, and dipole $Mn^{k+}$-$V_O$ defects [24]. Hence, the electrical features of PT were consistent with the reported $E_{gap}$ determined from the optical measurement and calculations mentioned above. The actual electronic structure of PT depends not only on defects concentration. Based on

doi:10.20944/preprints202110.0449.v1

density functional theory, calculated $E_{gap}$ changes from 3.18 to 3.03 eV, dependably on surface termination [25]. The FP-LAPW method calculation showed that absorption coefficient and energy gap decreased dependably on hydrostatic pressure [26].

BM crystal structure depends on growth conditions. Its perovskite meta-stable form, $BiMnO_3$, was only obtained when synthesis was performed under high hydrostatic pressure [27] and also by using the hydrothermal method [28]. When BM ceramics was sintered at standard high-temperature ambient air conditions, a thermodynamically stable two-phase self-composite compound was obtained. Two phases in equilibrium: the cubic *I*23 with the $Bi_{12}MnO_{20}$ composition and the orthorhombic *Pbam* with the $BiMn_2O_5$ composition, were determined. The self-composite BM was an electrically non-polar compound, which exhibited antiferromagnetic order in a low-temperature range with $T_{Néel} \approx 39$ K [29].

BM ceramics studied herein can be treated as a self-composite consisting of two phases. BM can be treated as a self-composite consisting of two phases. The $BiMn_2O_5$ phase exhibits calculated $E_{gap}$ = 0.78 eV [30] and the sillenite $Bi_{12}MnO_{20}$ exhibits intrinsic $E_{gap}$ = 1.86 eV [31]. In case of $BiMnO_3$ phase, $E_{gap}$ obtained from density of states (DOS) calculation was 0.33 eV, 0.3-0.4 eV, and ~1.1 eV [32–34]. BM exhibited semiconductor features and measured activation energy of electrical conductivity, which varied from $E_a$ = 0.13 eV and 0.20 eV to 0.32 eV when temperature increased from 120 K to 770 K [35]. Electrical conductivity was attributed to the polaronic mechanism, and simultaneously high values of permittivity occurred. What is more, the electrical conductivity relaxations, showing changeover to properties dominated by glassy features, were assigned to the strain-stress effect [36–39].

It is worth noting that BM-PT composite sintering in ambient air at high temperature resulted in mutual migration of ions that induced transformation of phases when the Pb and Ti ions of PT component diffused into the BM compound. Simultaneously, Bi and Mn migration affected the PT component [40,41]. For instance, it would be noted that the $Bi_2O_3$ phase, iso-structural with $Bi_{20}TiO_{32}$, transformed from the $Bi_{12}MnO_{20}$ parent phase of the BM self-composite. The $E_{gap}$ of the $Bi_2O_3$ compound varied from ~2 to ~3 eV dependably on technology [42,43].

The high magnitude electrical conductivity, permittivity, dielectric losses, relaxation processes behavior, and shortening relaxation times effects caused by external hydrostatic pressure and the stress field generated around the replaced ions, also observed for 0.96 BM–0.04 PT and 0.88 BM–0.12 PT composite ceramics, was reported in our previous papers [40,41]. The multiple states of $Mn^{2+}/Mn^{3+}/Mn^{4+}$ ions, which occur in the BM self-composite, may facilitate light absorption. Hence, the variance of phases should be considered as a possible origin of $E_{gap}$ tuning.

According to the literature, the optical $E_{gap}$ of the BM-PT composite components should be detected in different ranges of photon spectrum. The $E_{gap}$ = 3.4 eV of ideal stoichiometric PT corresponds to the ultraviolet range. The oxygen-deficient PT shows $E_{gap}$ = 2.6-2.9 eV in Vis range, the $E_{gap}$ = 1.86 eV of $Bi_{12}MnO_{20}$ relates to Vis range, and the $BiMn_2O_5$ $E_{gap}$ = 0.78 eV to NIR range. The ideal PT features are beyond our study frames. Contrary, the $E_{gap}$ of BM, BM-PT, and defected PT is to be tested in the Vis and the NIR range. Therefore, NIR energy spectrum analysis would detect energy levels induced by crystal lattice defects and doping.

A series of (1-$x$) BM–$x$ PT, ($x$ = 0.0, 0.02, 0.04, 0.08, 0.12, 0.16, 0.24) ceramics was sintered [39,41,44]. In this work, we studied diffused reflectance in the Vis-NIR range to determine the PT content influence on the BM-PT composite absorption coefficient and optical $E_{gap}$ magnitude. It should be noted that the photovoltaic efficiency also depends on properties of surface layer exposed to the incident light. Hence, we determined ceramics' morphology using scanning electron microscopy. Correspondence between light reflectance, estimated absorption coefficient, $E_{gap}$ magnitude, ceramics' morphology, their correspondence to electrical features, and possibilities of application of a BM-PT composite material are discussed in this manuscript.

## 2. Materials and Methods

### 2.1. Preparation of composite ceramics

Series of (1-$x$) BM–$x$ PT ($x$ = 0, 0.02, 0.04, 0.08, 0.12, 0.16, 0.24) ceramics was produced *via* standard high temperature sintering. A two-stage procedure was performed. BM ceramics [38] and PT powder [22] were prepared separately at the first step. BM ceramics were produced using high-temperature sintering in the air ($T_S$ = 1170 K for 2 h), according to the nominal $BiMnO_3$ formula [35]. They were graphite-like in color. The stoichiometric PT powder, which showed grains of sizes on submicron level (< 500nm), was obtained from the hydrothermal synthesis. It exhibited tetragonal *P*4*mm* symmetry [22]. The reference PT pellets were produced, and they were light yellow in color. Then the BM and PT powders were mixed in stoichiometric ratio, milled for 1 h, and pressed to pellets at 20 MPa. The ceramics were sintered at $T_S$ = 1170 K in ambient air for 1 h [40,41]. The sintered BM-PT ceramics were hard, porous, and graphite-like in color.

### 2.1. Vis-NIR reflectance

An USB-650 VIS-NIR Optic Spectrometer (OceanInsight, Inc., USA) equipped with a krypton light source lamp and OceanView 2.0 software was used. The Vis-NIR diffused reflectance, $R$, spectra of the samples were recorded in the wavelengths, $\lambda$, 400–1000 nm range at room temperature. The absorption coefficient was calculated from the reflectance spectra. The optical absorbance spectra were evaluated and presented using a Tauc plot of the modified Kubelka-Munk function to determine the optical band gap.

### 2.1. Surface morphology

A scanning microscope JSM-5410 equipped with an energy dispersion X-ray spectrometer (EDS with Si(Li) X-ray detector) was used to characterize the morphology and elemental content. The measuring chamber vacuum was $10^{-4}$ -$10^{-5}$ Pa.

## 3. Results

### 3.1. SEM morphology

The grains' morphology of series $x$ BM–(1-$x$) PT ceramics was studied by using SEM. The ceramics showed a variety of grain shapes: cubes, hexagon base polyhedrons, and tiny irregular forms. The voids and porosity were observed in ceramics surfaces.

Figure 1 shows secondary electron images obtained for the reference BM and PT ceramics. The BM map shows polyhedral-shaped hexagonal base grains with different sizes, varying predominantly in 0.2 – 2.0 µm in transverse dimension and 0.3 – 4.0 µm in longitudinal dimension, which is clearly visible in obtained polyhedrons grain size distribution (Figure 1a). There is a low amount of grains with longitudinal size above 6.0 µm. The PT ceramics shows homogenous morphology (Figure 1b). However, the grains' size is markedly smaller, lower than 1.0 µm.

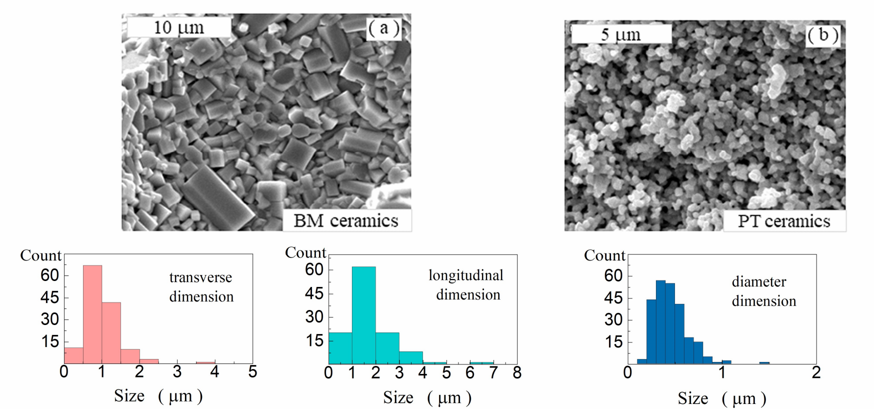

(a) (b)

**Figure 1**. Secondary electron images obtained for BM ceramics (a) and PT ceramics (b). Histograms show grains' transverse, longitudinal and diameter size distribution.

The 0.98 BM–0.02 PT ceramics (Figure 2a) shows variation in grains size similar to the pure BM ceramics. The obtained distribution shows that the grain' transverse dimension is mostly between 0.5 – 2.5 µm. The longitudinal dimension is mostly between 0.2 and 3.5 µm. There is a low amount of larger grains with sizes reaching 6.5 µm. On the contrary, the 0.96 BM–0.04 PT ceramics exhibits a higher amount of small grains (Figure 2b). Moreover, obtained grains size distributions show an increased number of larger size grains compared to the previous composition. Namely, grain' transverse dimension is mostly between 1.0 – 5.0 µm, and the longitudinal dimension is mostly between 0.5 and 4.0 µm. There are several large grains with longitudinal sizes above 10.0 µm.

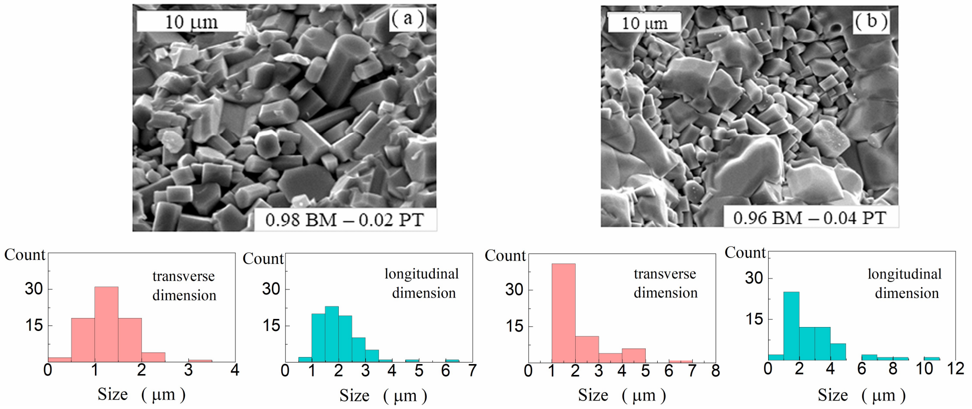

(a) (b)

**Figure 2**. Secondary electron images obtained for 0.98 BM–0.02 PT ceramics (a) and 0.96 BM–0.04 PT ceramics (b). Histograms show grains' transverse and longitudinal size distribution.

Figure 3a and 3b show similar morphology of 0.92 BM–0.08 PT and 0.88 BM–0.12 PT ceramics, respectively. The obtained histograms show that the amount of the grain' of transverse varies between 0.3 – 3.0 µm for both ceramics. The longitudinal dimension distribution is slightly different when compared for these two ceramics and varies between 1.0 – 5.5 µm for 0.92 BM–0.08 PT and 1.0 – 4.5 µm for the 12 % of PT. There are no large grains with longitudinal size above 6.0 µm, which occur for the ceramics with a low amount of dopant PT (compare Figure 2 and Figure 3).

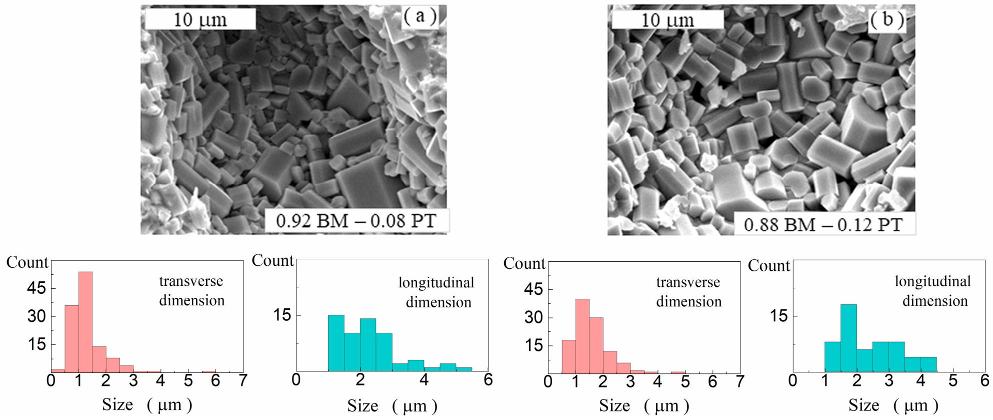

(a) (b)

**Figure 3**. Secondary electron images obtained for 0.92 BM–0.08 PT ceramics (a) and 0.88 BM–0.12 PT ceramics (b). Histograms show grains' transverse and longitudinal size distribution.

The obtained results for the high contents of PT are shown in Figure 4a and 4b. We can see that the 0.84 BM–0.16 PT structure contains both large and tiny grains. The transverse size of the grain is mostly between 0.3 and 2.0 µm. Moreover, there are grains, which dimensions reach 7.0 µm. Grains' longitudinal dimensions vary from 0.2 µm to 12.0 µm (Figure 4a). In turn, the 0.76 BM–0.24 PT transverse size is mostly between 0.5 and 3.0 µm, while the grains' longitudinal size is between 1.0 and 5.5 µm (Figure 4b).

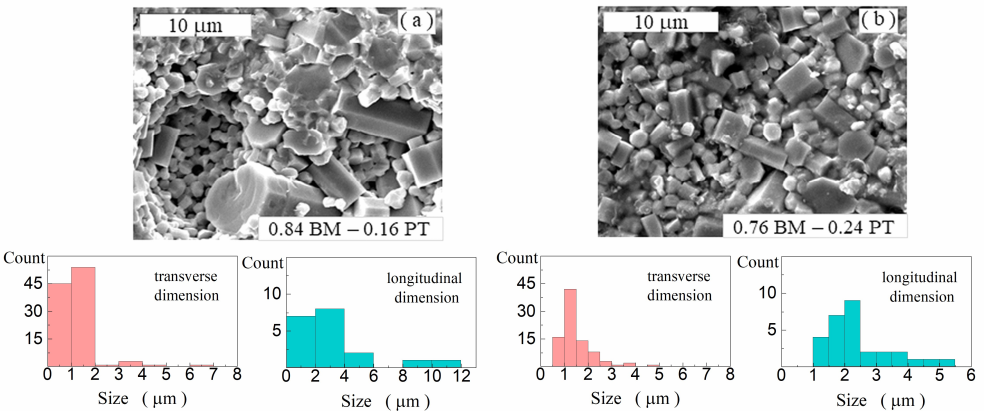

(a) (b)

**Figure 4**. Secondary electron images obtained for 0.84 BM–0.16 PT ceramics (a) and 0.76 BM–0.24 PT ceramics (b). Histograms show grains' transverse and longitudinal size distribution.

The studied herein ceramic composites exhibit many caverns in the fracture surfaces (Figure 5). Such cavities are typical for the reference bismuth manganate ceramics [35]. Their origin would be associated with the technological process and attributed to chemical reactions. The occurrence of these cavities, where well-formed grains are visible, is one common feature of the BM-PT ceramics. The other common feature is porosity. We can distinguish well-shaped hexagon base polyhedrons grains, which are loosely attached each to other. Any clear tendency in size grain distribution in respect to PT content contribution was not observed for the BM-PT composite series. The majority of grains exhibited transverse size, which did not exceed 2.0 µm. The main amount of grains showed longitudinal size lower than 7.0 µm. The exception occurred for 0.96 BM–0.04 PT and 0.84 BM–0.16 PT composition, where longitudinal size reached dimension up to 12.0 µm. We attributed the occurrence of the small amount of grains of size below 1.0 µm to the presence of the PT compound in the ceramics composite that is clearly visible for ceramics with higher content of PT.

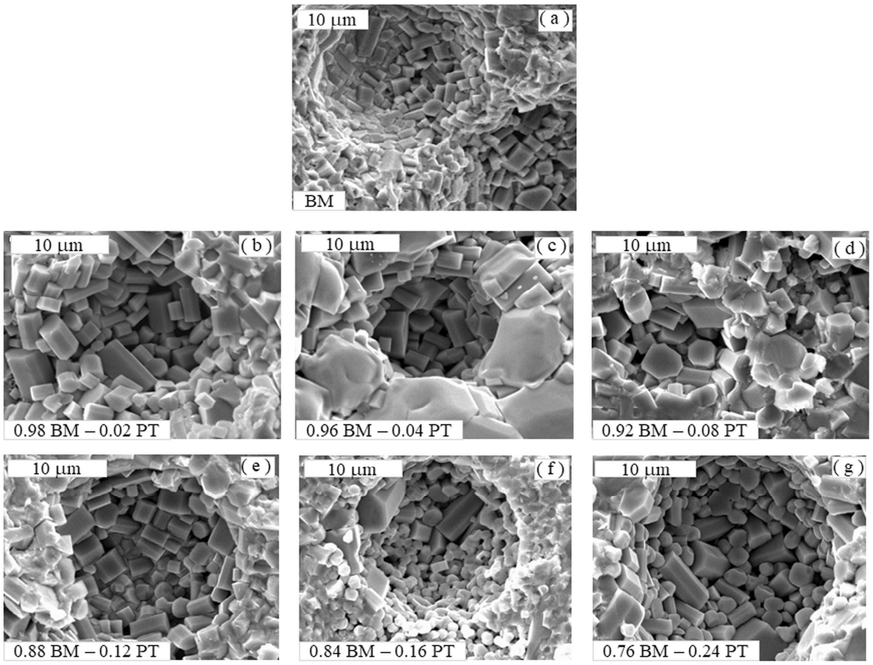

**Figure 5**. Secondary electron images obtained for the composite ceramics: BM (a), 0.98 BM–0.02 PT (b), 0.96 BM–0.04 PT (c), 0.92 BM–0.08 PT (d), 0.88 BM–0.12 PT (e), 0.84 BM–0.16 PT (e), and 0.76 BM–0.24 PT (f).

### 3.2. *Vis-NIR optical features*

The room temperature diffused reflectance, *R*, spectra were measured in 400–1000 nm range, which included Vis–NIR spectrum. For the graphical estimation of the $E_{gap}$ magnitude, the Vis–NIR spectra recorded in the *R* mode were transformed to Kubelka-Munk function,

$$F(R) = (1-R)^2/2R, \tag{1}$$

which is proportional to the extinction coefficient, $\alpha$. Determination of $E_{gap}$ was conducted using the Tauc method and relation of incident photon energy, $E = h\nu$, with the modified Kubelka-Munk function:

$$\alpha\cdot h\nu \approx B(h\nu - E_{gap})^n. \tag{2}$$

We presumed the indirect allowed transitions in the BM-PT composite. Hence, $\alpha(h\nu)^{1/n}$ versus $h\nu$ plots, where exponent $n = 2$, were applied for analysis. The $E_{gap}$ value was obtained by extrapolating the straight-line segment to the intersection with the $h\nu$ axis, that is for $\alpha(h\nu)^{1/2} = 0$ [45]. We performed such extrapolation fit both for NIR and Vis range, where flat slopes could be distinguished. Such an approach was justified because of the multi-phase structure of studied herein composites.

We note that the PT, $BiMn_2O_5$, $Bi_{12}MnO_{20}$, and their derivative phases, which resulted from sintering, would bring in individual electronic structure contributions. In the case of composite, doped, defected, and multi-phase materials, the resulting spectra can include contributions from particular energy gaps. Such modifications may introduce intraband gap states that reflect in the reflectance an additional band. A spectrum of any mixture, including a doping-modified and two-phase semiconductor, is the linear combination of the spectra of both components;

$$(\alpha(h\nu))_{eff} = a\cdot\alpha_1(h\nu) + b\cdot\alpha_2(h\nu)), \tag{3}$$

where a and b determine the components' concentrations contributions, while $\alpha_1$(hν) and $\alpha_2$(hν) are the absorption coefficients of the assumed two phases contribution.

The determination of energy gaps related to particular phases causes a dilemma of accuracy Tauc equation reads:

$$\{ [\, a\cdot \alpha_1(h\nu) + b\cdot \alpha_2(h\nu)]\cdot h\nu \,\}^{1/2} = B(h\nu - E_{gap}), \quad (4)$$

and direct application of the Tauc method brings in a systematic shift in the estimated $E_{gap}$ magnitude [46]. However, as the needed approximation, we decided to conduct the spectra analysis using Tauc method independently for the NIR and Vis range, respectively. Such an approach was justified by the occurrence of at least two phases, which properties would determine $R$ magnitude in the NIR and the Vis range, respectively.

The diffused reflectance spectra of BM and PT reference ceramics are shown in Figure 6. The $R(\lambda)$ increased when wavelength increased, more steeply for $\lambda > 900$ nm. A broad hump occurred in ~550-800 nm range, which corresponded to red and dark red light. The most distinct difference occurred in 400-550 nm range, where PT reflectance exhibited steep change in $R$ magnitude, contrary to the BM sample.

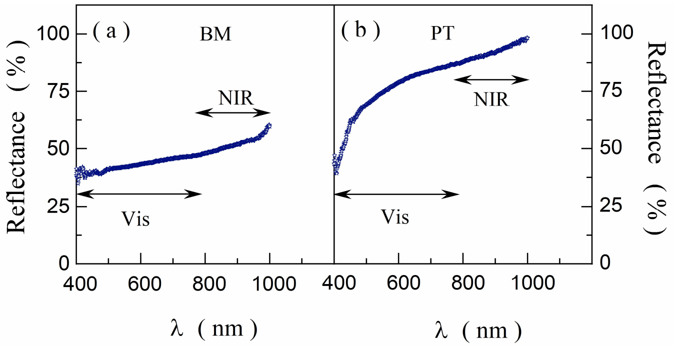

(a) (b)

**Figure 6**. Reflectance, $R$, *vs*. wavelengths, $\lambda$, dependence measured for BM (a) and PT (b).

We discerned the straight-line segments in the modified Kubelka-Munk function plot obtained for the reference BM self-composite. $E_{gap}$(NIR) = 1.25 eV was estimated for the NIR range (Figure 7a). $E_{gap}$(NIR) = 1.25 eV was estimated in case of the reference PT compound. Moreover, fitting of two straight-line segments were in Vis range was possible. The $E_{gap,1}$(Vis) = 1.5 eV and $E_{gap,2}$(Vis) = 2.45 eV was obtained, respectively (Figure 7b).

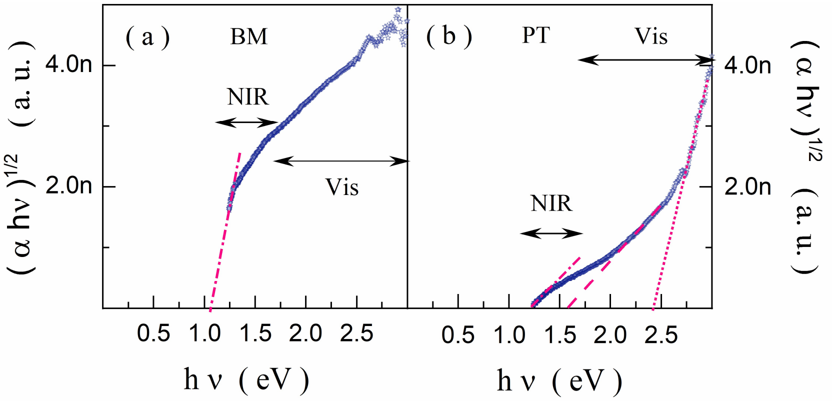

(a) (b)

**Figure 7**. Modified Kubelka-Munk function $(\alpha h\nu)^{1/2}$ *vs*. photon energy $h\nu$ plot obtained for BM (a) and PT (b).

$R(\lambda)$ spectra obtained for (1-$x$) BM–$x$ PT composites are shown in Figure 8. $R$ magnitude decreased when the PT content increased, from ~50-60 % to ~25-30 % despite that the reference PT $R(\lambda)$ varied in 40-100 % range (compare Figures 6 and 8). The $R(\lambda)$ common feature was its magnitude increase when wavelength increased and more steep change in $R$ magnitude for $\lambda > 900$ nm. A more or less distinct broad hump occurred in ~550-800 nm range, it shifted toward NIR range and became negligible for high content of PT component.

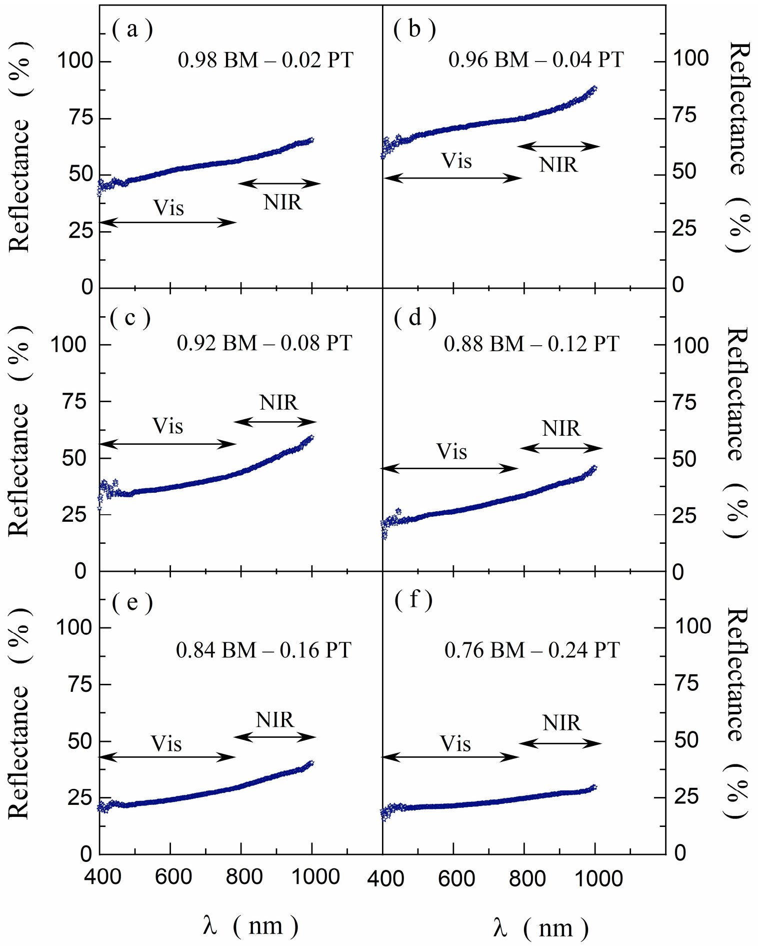

**Figure 8**. Reflectance, $R$, *vs*. wavelengths, $\lambda$, dependence measured for (1-$x$) BM–$x$ PT ceramics, $x$ = 0.02, 0.04, 0.08, 0.12, 0.16, 0.24, (a) – (f), respectively.

Graphical representation of modified Kubelka–Munk function allowed us to determine $E_{gap}$ magnitude dependence on the (1-$x$) BM–$x$ PT ceramics composition (Figure 9). We discerned straight-line segments in the $(\alpha h\nu)^{1/2}$ *vs*. $h\nu$ plots, both in Vis and NIR range, because of the presumed manifestation of the multi-phase (1-$x$) BM–$x$ PT ceramics features.

The $E_{gap}$ of the order of ~1 eV was estimated from the Vis spectrum range and it showed a tendency to fluctuate with PT content change. The $E_{gap}$ of ~0.13-0.36 eV estimated from the NIR range also fluctuated with PT content increase. The variation of the estimated gap energies versus the PT content, $x$, is shown in Figure 10.

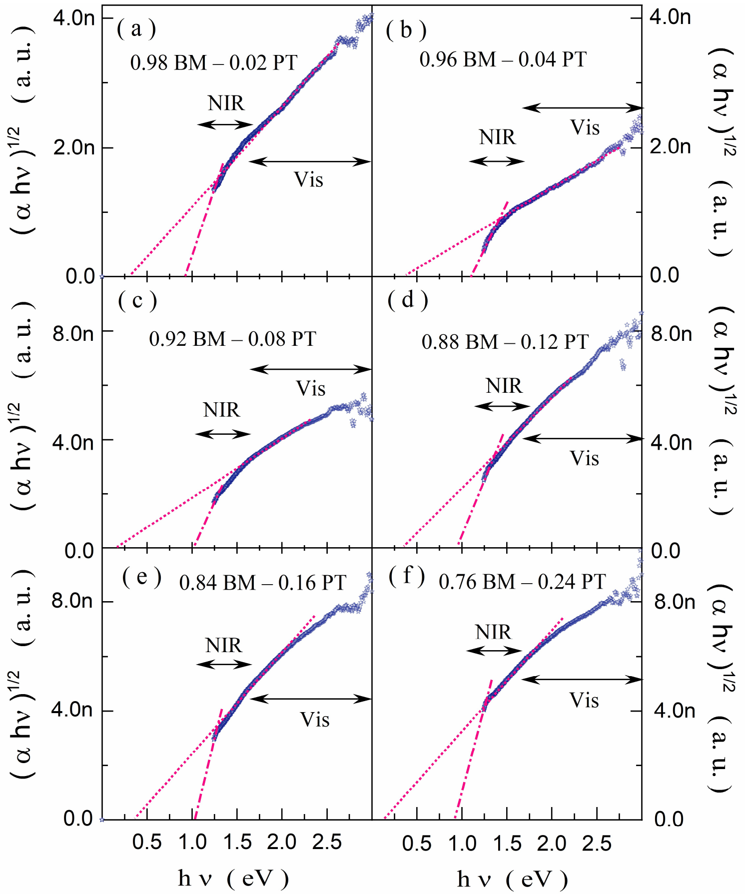

**Figure 9.** Modified Kubelka-Munk function $(\alpha h\nu)^{1/2}$ *vs*. photon energy $h\nu$ plot obtained for (1-$x$) BM–$x$ PT ceramics, $x$ = 0.02, 0.04, 0.08, 0.12, 0.16, 0.24, (a) –(f), respectively.

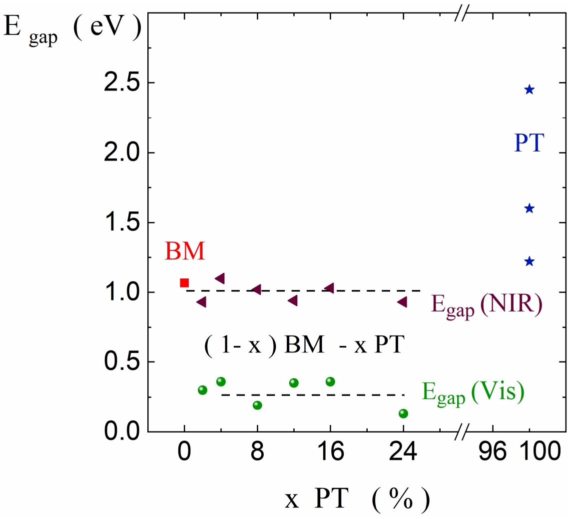

**Figure 10**. Optical energy gaps estimated for BM, PT, and (1-$x$) BM–$x$ PT ceramic composites ($x$ = 0.02, 0.04, 0.08, 0.12, 0.16, and 0.24).

## 4. Discussion

The BM and BM-PT ceramics are multi-phase composites [35,38,47]. BM is the self-composite consisting of the major $BiMn_2O_5$ and the minor $Bi_{12}MnO_{20}$ phase. The BM-PT composite consists of phases, which structure changed because of mutual migration of ions when the ceramics were sintered from the reference BM and PT [40,41]. Moreover, local fluctuations in composition and the occurrence of oxygen deficiency cannot be excluded. The graphite-black color of these compounds indicated light absorbance in Vis and NIR range. Hence, $E_{gap}$ lower than ~1.5 eV was expected. Contrary, the reference PT powder was the one-phase compound. The light-yellow color of this material suggested that the actual $E_{gap}$ magnitude, originated from a defected PT structure, would be lower from $E_{gap}$ = 3.4 eV reported for the ideal stoichiometric transparent crystal [18,19].

Therefore, the measured $R(\lambda)$ spectra were considered as effective quantities, which included contributions from individual phases of the BM-PT system. It should be noted that when the PT content in the BM-PT ceramics was higher, the lower $R$ magnitude occurred. The $R$ magnitude decrease from ~50-60% to ~25-30 % indicated the active role of the PT component and marked influence porosity. A standard flat and smooth surface, like a glassy black mirror, usually offers reflectance on 40-50% level. Lower reflectance would be achieved in the case of a textured surface when light is scattered and absorbed more effectively [48]. It should be noticed that the SEM test exhibited porosity and concave voids in the BM-PT ceramics surfaces. Therefore, despite any uncontrolled and random factor which cannot be excluded a priori, we deduce that that the low reflectance of the BM-PT ceramics can relate to the rough surface features.

Grain size also is one of the factors, which affect the photo-voltaic properties. The correlation between the increasing grain size, within the sub-micro range, and $E_{gap}$ magnitude increase was reported for perovskite materials [49]. However, in our studies any marked tendency in the BM-PT grain size was not determined (see Figures 1-5). On the other hand, we note that the reference PT powder grain was much smaller than the BM-PT compounds grain (compare Figure 1b to Figures 1a and 2-5). Hence, we deduce that tiny grains of the PT powder introduced to the sintered BM-PT ceramics also would be responsible for this effect. Hence, we conclude that both the small grains of the PT component and the porous texture of BM-PT ceramics surface may facilitate scattering, decrease reflectance to ~25%, and enhance light absorption.

We applied the Tauc procedure independently within the NIR and the Vis range. We followed the idea that particular phases of a composite can independently contribute to the overall effective reflectance spectrum.

The estimated $E_{gap}$(NIR) magnitude, which fluctuated on 1.00±0.10 eV level was obtained both for the BM and the BM-PT compounds. It correlates to the $E_{gap}$ = 0.78 eV calculated for the major $BiMn_2O_5$ orthorhombic *Pbam* phase of the BM composite [30]. The correspondence to $E_{gap}$ = 1.10 eV seems to less valid because of the other, monoclinic structure of $BiMnO_3$ phase considered for this calculation [34]. The other $E_{gap}$ magnitude was determined for BM-PT composites in the Vis range. The estimated $E_{gap}$(Vis) fluctuated in 0.13-0.36 eV range when the PT content increased, showing no clear tendency. Such narrow $E_{gap}$ corresponds to the measured activation energy of electrical conductivity at room temperature reported in literature: $E_a$ = 0.20 eV [35], and 0.24 eV for BM [39] and 0.34-0.40eV for BM-PT compounds [40,41]. The correspondence to the $E_{gap}$ = 0.33 eV calculated for the stoichiometric $BiMnO_3$ [32] and $E_{gap}$ = 0.45eV calculated for the oxygen-deficient $BiMnO_{3-x}$ [34] should also be noticed.

In the case of reference PT, determination of three different $E_{gap}$ magnitudes were proposed. The $E_{gap,1}$(Vis) = 1.5 eV and $E_{gap,2}$(Vis) = 2.45 eV was estimated for the intermediate orange - cyan light and blue-light Vis range, respectively. These result correspond to the literature data, $E_{gap}$ =1.3-2.5 eV [22] and $E_{gap}$ = 2.6 eV [21], were reported for the defected PT crystals. The $E_{gap}$(NIR) = 1.25 eV corresponds to the $E_a$ = 1.3 eV of electrical conductivity measured for the pellets obtained from the same PT powders [22]. One also can notice coincidence to the obtained from calculation additional states lying 1.1 eV below the Fermi energy within energy gap, which were attributed to $V_O$ defects occurrence

[20]. Hence, such the coincidence suggest that participation of PT originated $E_{gap}$(NIR) in the effective $R(\lambda)$ spectra might be justified. Therefore, $V_O$ defects and other crystal lattice defects influence on the measured actual $R(\lambda)$ spectrum and the determined $E_{gap}$ magnitude cannot be excluded.

In short summary, BM-PT composite ceramics show features interesting for photovoltaic application:
(1) BM-PT rough surfaces provide low reflectance and high absorption efficiency;
(2) Estimated $E_{gap}$ magnitude, lower than 1.5 eV, corresponds to light absorption in NIR range;
(3) $E_{gap}$ magnitude of the order of 0.2 eV correlates to activation energies determined for the electrical conductivity.

**Author Contributions:** Conceptualization, A.M.; methodology, A.M, A.Z.S, J.K.; validation, A.M, A.Z.S. J.K.; formal analysis, A.M, A.Z.S; investigation, A.M, A.Z.S, J.K.; writing—original draft preparation, A.M.; writing—review and editing, A.M, A.Z.S.; visualization, A.M, A.Z.S.; funding acquisition, A.M, A.Z.S.

**Funding:** A. Molak and A. Z. Szeremeta note that this publication is co-financed by the funds granted under the Research Excellence Initiative of the University of Silesia in Katowice.

**Conflicts of Interest:** The authors declare no conflict of interest.

## References

1. Li, S.; Morasch, J.; Klein, A.; Chirila, C.; Pintilie, L.; Jia, L.; Ellmer, K.; Naderer, M.; Reichmann, K.; Gröting, M.; et al. Influence of orbital contributions to the valence band alignment of $Bi_2O_3$, $Fe_2O_3$, $BiFeO_3$, and $Bi_{0.5}Na_{0.5}TiO_3$. *Phys. Rev. B* **2013**, *88*, 045428, doi:10.1103/PhysRevB.88.045428.
2. Li, P.; Abe, H.; Ye, J. Band-Gap Engineering of $NaNbO_3$ for Photocatalytic $H_2$ Evolution with Visible Light. *Int. J. Photoenergy* **2014**, *2014*, 1–6, doi:10.1155/2014/380421.
3. Hwang, D.W.; Kim, H.G.; Lee, J.S.; Kim, J.; Li, W.; Oh, S.H. Photocatalytic Hydrogen Production from Water over M-Doped $La_2Ti_2O_7$ (M = Cr, Fe) under Visible Light Irradiation ($\lambda > 420$ nm). *J. Phys. Chem. B* **2005**, *109*, 2093–2102, doi:10.1021/jp0493226.
4. Wang, D.; Ye, J.; Kako, T.; Kimura, T. Photophysical and Photocatalytic Properties of $SrTiO_3$ Doped with Cr Cations on Different Sites. *J. Phys. Chem. B* **2006**, *110*, 15824–15830, doi:10.1021/jp062487p.
5. Bujakiewicz-Koronska, R.; Nalecz, D.M.; Molak, A.; Budziak, A. DOS calculation for stoichiometric and oxygen defected $(Bi_{1/2}Na_{1/2})(Mn_{1/2}Nb_{1/2})O_3$. *Ferroelectrics* **2014**, *463*, 48–56, doi:10.1080/00150193.2014.891918.
6. Shi, H.; Li, X.; Iwai, H.; Zou, Z.; Ye, J. 2-Propanol photodegradation over nitrogen-doped $NaNbO_3$ powders under visible-light irradiation. *J. Phys. Chem. Solids* **2009**, *70*, 931–935, doi:10.1016/j.jpcs.2009.05.002.
7. Zheng, D.; Deng, H.; Pan, Y.; Guo, Y.; Zhao, F.; Yang, P.; Chu, J. Modified multiferroic properties in narrow bandgap $(1-x)BaTiO_3$-$xBaNb_{1/3}Cr_{2/3}O_{3-\delta}$ ceramics. *Ceram. Int.* **2020**, *46*, 26823–26828, doi:10.1016/j.ceramint.2020.07.158.
8. Prosandeyev, S.A.; Teslenko, N.M.; Fisenko, A. V Breaking of symmetry of one-electron orbitals at oxygen vacancies in perovskite-type oxides. *J. Phys. Condens. Matter* **1993**, *5*, 9327–9344, doi:10.1088/0953-8984/5/50/014.
9. Gadhoumi, F.; Kallel, I.; Benzarti, Z.; Abdelmoula, N.; Hamedoun, M.; Elmoussaoui, H.; Mezzane, D.; Khemakhem, H. Investigation of magnetic, dielectric and optical properties of $BiFe_{0.5}Mn_{0.5}O_3$ multiferroic ceramic. *Chem. Phys. Lett.* **2020**, *753*, 137569, doi:10.1016/j.cplett.2020.137569.
10. Molak, A.; Pilch, M. Visible light absorbance enhanced by nitrogen embedded in the surface layer of Mn-doped sodium niobate crystals, detected by ultra violet - visible spectroscopy, x-ray photoelectron spectroscopy, and electric conductivity tests. *J. Appl. Phys.* **2016**, *119*, 204901, doi:10.1063/1.4948937.
11. Mefford, J.T.; Hardin, W.G.; Dai, S.; Johnston, K.P.; Stevenson, K.J. Anion charge storage through oxygen intercalation in $LaMnO_3$ perovskite pseudocapacitor electrodes. *Nat. Mater.* **2014**, *13*, 726–732, doi:10.1038/nmat4000.

12. Huang, Y.; Wei, Y.; Cheng, S.; Fan, L.; Li, Y.; Lin, J.; Wu, J. Photocatalytic property of nitrogen-doped layered perovskite $K_2La_2Ti_3O_{10}$. *Sol. Energy Mater. Sol. Cells* **2010**, *94*, 761–766, doi:10.1016/j.solmat.2009.12.020.
13. Srivastava, S. Study of Band Gap Tunablity in one-dimensional Photonic Crystals of Multiferroic-dielectric materials: Case Study in Near Infrared Region. *SOP Trans. Appl. Phys.* **2014**, *2014*, 22–32, doi:10.15764/APHY.2014.01005.
14. Benjwal, P.; Kar, K.K. Removal of methylene blue from wastewater under a low power irradiation source by Zn, Mn co-doped $TiO_2$ photocatalysts. *RSC Adv.* **2015**, *5*, 98166–98176, doi:10.1039/C5RA19353B.
15. Ma, X.; Yang, L.; Lei, K.; Zheng, S.; Chen, C.; Song, H. Doping in inorganic perovskite for photovoltaic application. *Nano Energy* **2020**, *78*, 105354, doi:10.1016/j.nanoen.2020.105354.
16. Waldmeyer, J. A contactless method for determination of carrier lifetime, surface recombination velocity, and diffusion constant in semiconductors. *J. Appl. Phys.* **1988**, *63*, 1977–1983, doi:10.1063/1.341097.
17. Peng, Q.; Weng, X.; Xie, W.; Ying, M.; Lin, X.; Dai, Y.; Yu, Q.; Pan, H.; Liu, J.; Du, M. Photocatalytic reduction for graphene oxide by $PbTiO_3$ with high polarizability and its electrocatalytic application in pyrrole detection. *J. Colloid Interface Sci.* **2020**, *560*, 502–509, doi:10.1016/j.jcis.2019.10.022.
18. Niu, P.J.; Yan, J.L.; Xu, C.Y. First-principles study of nitrogen doping and oxygen vacancy in cubic $PbTiO_3$. *Comput. Mater. Sci.* **2015**, *98*, 10–14, doi:10.1016/j.commatsci.2014.10.057.
19. Zametin, V.I. Absorption Edge Anomalies in Polar Semiconductors and Dielectrics at Phase Transitions. *Phys. status solidi* **1984**, *124*, 625–640, doi:10.1002/pssb.2221240222.
20. Cai, M.-Q.; Tang, C.-H.; Tan, X.; Deng, H.-Q.; Hu, W.-Y.; Wang, L.-L.; Wang, Y.-G. First-principles study for the atomic structures and electronic properties of $PbTiO_3$ oxygen-vacancies (001) surface. *Surf. Sci.* **2007**, *601*, 5412–5418, doi:10.1016/j.susc.2007.08.026.
21. Gerges, M.K.; Mostafa, M.; Rashwan, G.M. Structural, optical and electrical properties of PbTiO3 nanoparticles prepared by Sol-Gel method. *Int. J. Latest Res. Eng. Technol.* **2016**, *2*, 42–49.
22. Leonarska, A.; Ujma, Z.; Molak, A. Nano-size grain powders and ceramics of $PbTiO_3$ obtained by the hydrothermal method and their electrical properties. *Ferroelectrics* **2014**, *466*, 42–50, doi:10.1080/00150193.2014.894861.
23. Pilch, M.; Molak, A. Resistivity switching induced in ferroelectric phase of $PbTiO_3$ studied by XPS and electric conductivity tests. *J. Alloys Compd.* **2014**, *586*, 488–498, doi:10.1016/j.jallcom.2013.10.103.
24. Molak, A.; Wöjcik, K. Optic properties and EPR spectra of $PbTiO_3$:Mn crystals. *Ferroelectrics* **1992**, *125*, 349–354, doi:10.1080/00150199208017092.
25. de Lazaro, S.; Longo, E.; Sambrano, J.R.; Beltrán, A. Structural and electronic properties of $PbTiO_3$ slabs: a DFT periodic study. *Surf. Sci.* **2004**, *552*, 149–159, doi:10.1016/j.susc.2004.01.041.
26. Yaseen, M.; Ambreen, H.; Mehmood, R.; Iqbal, M.; Iqbal, J.; Alshahrani, T.; Noreen, S.; Laref, A. Investigation of optical and thermoelectric properties of $PbTiO_3$ under pressure. *Phys. B Condens. Matter* **2021**, *615*, 412857, doi:10.1016/j.physb.2021.412857.
27. Belik, A.A. Polar and nonpolar phases of $BiMO_3$: A review. *J. Solid State Chem.* **2012**, *195*, 32–40, doi:10.1016/j.jssc.2012.01.025.
28. Samuel, V.; Navale, S.C.; Jadhav, A.D.; Gaikwad, A.B.; Ravi, V. Synthesis of ultrafine $BiMnO_3$ particles at 100 °C. *Mater. Lett.* **2007**, *61*, 1050–1051, doi:10.1016/j.matlet.2006.06.046.
29. Muñoz, A.; Alonso, J.A.; Casais, M.T.; Martínez-Lope, M.J.; Martínez, J.L.; Fernández-Díaz, M.T. Magnetic structure and properties of $BiMn_2O_5$. *Phys. Rev. B* **2002**, *65*, 144423, doi:10.1103/PhysRevB.65.144423.
30. Zhang, J.; Xu, B.; Li, X.F.; Yao, K.L.; Liu, Z.L. Origin of the multiferroicity in $BiMn_2O_5$ from first-principles calculations. *J. Magn. Magn. Mater.* **2011**, *323*, 1599–1605, doi:10.1016/j.jmmm.2010.12.040.
31. Wu, X.; Li, M.; Li, J.; Zhang, G.; Yin, S. A sillenite-type $Bi_{12}MnO_{20}$ photocatalyst: UV, visible and infrared lights responsive photocatalytic properties induced by the hybridization of Mn 3d and O 2p orbitals. *Appl. Catal. B Environ.* **2017**, *219*, 132–

141, doi:10.1016/j.apcatb.2017.07.025.

32. McLeod, J.A.; Pchelkina, Z. V.; Finkelstein, L.D.; Kurmaev, E.Z.; Wilks, R.G.; Moewes, A.; Solovyev, I. V.; Belik, A.A.; Takayama-Muromachi, E. Electronic structure of $BiMO_3$ multiferroics and related oxides. *Phys. Rev. B* **2010**, *81*, 144103, doi:10.1103/PhysRevB.81.144103.
33. Bujakiewicz-Koronska, R.; Nalecz, D.M.; Bałanda, M.; Molak, A.; Ujma, Z. Electronic and magnetic properties of $(Bi_{0.5}Na_{0.5})(Mn_{0.5}Nb_{0.5})O_3$. *Phase Transitions* **2014**, *87*, 1096–1104, doi:10.1080/01411594.2014.953506.
34. Bujakiewicz-Koronska, R.; Nalecz, D.M. First principles calculations of ideal and defected $BiMnO_3$. *Phase Transitions* **2013**, *86*, 167–174, doi:10.1080/01411594.2012.728399.
35. Molak, A.; Ujma, Z.; Pilch, M.; Gruszka, I.; Pawelczyk, M. Resistance switching induced in $BiMnO_3$ ceramics. *Ferroelectrics* **2014**, *464*, 59–71, doi:10.1080/00150193.2014.892815.
36. Chiba, H.; Atou, T.; Syono, Y. Magnetic and Electrical Properties of $Bi_{1-x}Sr_xMnO_3$: Hole-Doping Effect on Ferromagnetic Perovskite $BiMnO_3$. *J. Solid State Chem.* **1997**, *132*, 139–143, doi:10.1006/jssc.1997.7432.
37. Belik, A.A.; Iikubo, S.; Yokosawa, T.; Kodama, K.; Igawa, N.; Shamoto, S.; Azuma, M.; Takano, M.; Kimoto, K.; Matsui, Y.; et al. Origin of the monoclinic-to-monoclinic phase transition and evidence for the centrosymmetric crystal structure of $BiMnO_3$. *J. Am. Chem. Soc.* **2007**, *129*, 971–977, doi:10.1021/ja0664032.
38. Molak, A.; Leonarska, A.; Szeremeta, A. Electric current relaxation and resistance switching in non-homogeneous bismuth manganite. *Ferroelectrics* **2015**, *485*, 161–172, doi:10.1080/00150193.2015.1061868.
39. Szeremeta, A.Z.; Pawlus, S.; Nowok, A.; Grzybowska, K.; Zubko, M.; Molak, A. Hydrostatic pressure influence on electric relaxation response of bismuth manganite ceramics. *J. Am. Ceram. Soc.* **2020**, *103*, 3732–3738, doi:10.1111/jace.17054.
40. Molak, A.; Szeremeta, A.Z.; Zubko, M.; Nowok, A.; Balin, K.; Gruszka, I.; Pawlus, S. Influence of hydrostatic pressure on electrical relaxation in non-homogeneous bismuth manganite - Lead titanate ceramics. *J. Alloys Compd.* **2021**, *854*, 157219, doi:10.1016/j.jallcom.2020.157219.
41. Szeremeta, A.Z.; Nowok, A.; Zubko, M.; Pawlus, S.; Gruszka, I.; Koperski, J.; Molak, A. Influence of interfacial stresses on electrical properties of bismuth manganite – lead titanate – epoxy composite. *Ceram. Int.* **2021**, doi:10.1016/j.ceramint.2021.08.376.
42. Ho, C.-H.; Chan, C.-H.; Huang, Y.-S.; Tien, L.-C.; Chao, L.-C. The study of optical band edge property of bismuth oxide nanowires $\alpha$-$Bi_2O_3$. *Opt. Express* **2013**, *21*, 11965, doi:10.1364/OE.21.011965.
43. Vila, M.; Díaz-Guerra, C.; Piqueras, J. Luminescence and Raman study of $\alpha$-$Bi_2O_3$ ceramics. *Mater. Chem. Phys.* **2012**, *133*, 559–564, doi:10.1016/j.matchemphys.2012.01.088.
44. Szeremeta, A.Z. Doctoral Thesis (in Polish language), University of Silesia, Katowice, 2018.
45. López, R.; Gómez, R. Band-gap energy estimation from diffuse reflectance measurements on sol–gel and commercial $TiO_2$: a comparative study. *J. Sol-Gel Sci. Technol.* **2012**, *61*, 1–7, doi:10.1007/s10971-011-2582-9.
46. Makuła, P.; Pacia, M.; Macyk, W. How To Correctly Determine the Band Gap Energy of Modified Semiconductor Photocatalysts Based on UV–Vis Spectra. *J. Phys. Chem. Lett.* **2018**, *9*, 6814–6817, doi:10.1021/acs.jpclett.8b02892.
47. Pilch, M.; Molak, A.; Koperski, J.; Zajdel, P. Influence of nitrogen flow during sintering of bismuth manganite ceramics on grain morphology and surface disorder. *Phase Transitions* **2017**, *90*, 112–124, doi:10.1080/01411594.2016.1219737.
48. Zhong, J.; Wu, W.; Liao, J.; Feng, W.; Jiang, Y.; Wang, L.; Kuang, D. The Rise of Textured Perovskite Morphology: Revolutionizing the Pathway toward High-Performance Optoelectronic Devices. *Adv. Energy Mater.* **2020**, *10*, 1902256, doi:10.1002/aenm.201902256.
49. Niloy, N.R.; Chowdhury, M.I.; Anowar, S.; Islam, J.; Rhaman, M.M. Structural and Optical Characterization of Multiferroic $BiFeO_3$ Nanoparticles Synthesized at Different Annealing Temperatures. *J. Nano- Electron. Phys.* **2020**, *12*, 05015-1-05015–6, doi:10.21272/jnep.12(5).05015.